Binocular vision measurement system for geometric error of 3D printers at high temperature

Rui Li[1] · Nuodi Huang[1] · Yang Zhang[1] · Limin Zhu[1] · Soichi Ibaraki[2]

Received: 6 November 2023 / Accepted: 2 December 2023 / Published online: 20 December 2023

Abstract
The accuracy of material extrusion-based 3D printers is greatly affected by the high temperature in the chamber due to the thermal-induced deformation of components. However, most existing measurement equipment cannot be applied to high-temperature environments, which hinders the corresponding error measurement. To address this issue, a geometric error detection system and identification algorithm based on binocular vision are proposed. Firstly, a corner detection algorithm and a ray-intersection binocular model are used to identify the three-dimensional displacement of the target. Secondly, an error separation and identification algorithm is proposed to identify 21 position-dependent geometric errors. Error measurement experiments are conducted on a 3D printer at room temperature and high temperature, respectively. The experimental results at room temperature are verified using a double-ball bar. Finally, an error compensation experiment is conducted to verify the effectiveness of error identification, which also shows the contribution of error motions of linear axes on the printing accuracy.

Keywords Vision measurement · High-temperature measurement · Position-dependent geometric errors · 3D printer · Geometric error identification

1 Introduction

Additive manufacturing plays an important role in prototype manufacturing and non-metallic processing. As the main equipment for additive manufacturing, the machining accuracy of 3D printers directly affects the quality of the final workpiece. Geometric errors have a significant effect on the accuracy of 3D printers [1]. And error measurement is the precondition and foundation of error compensation. Unlike conventional machine tools, material extrusion-based 3D printers work under high-temperature conditions (90 ~ 320 ℃), which contributes greatly to the geometric error of the device and makes geometric error measurement quite difficult [2]. Therefore, fast and accurate measurement of geometric errors in a 3D printer is already an urgent research issue to be solved.

Error modeling is important for the measurement and compensation of geometric errors, and there are numerous relevant research results, including multi-body system theory, screw theory [3], and exponential product method [4]. Among them, the multi-body system theory has been broadly accepted. In this theory, the device is modeled as a multi-body topological system [5]. According to their correlation with the position, geometric errors could be categorized into position-dependent geometric errors (PDGEs) and position-independent geometric errors (PIGEs) [6]. A great deal of research has been carried out on geometric error measurement, and many related instruments and methods have been produced.

In the application scenarios of geometric error measurement, the most commonly used instruments currently include laser interferometer [7], laser tracker [8], and double-ball bar (DBB) [9]. The measurement based on a laser interferometer is a classical method to identify the geometric errors of machine tools. Paweł et al. used a laser interferometer to quantify the displacement during the uninterrupted movement of the axis, enabling a dynamic assessment of the

✉ Nuodi Huang
nhuang@sjtu.edu.cn

[1] State Key Laboratory of Mechanical System and Vibration, School of Mechanical Engineering, Shanghai Jiao Tong University, Shanghai 200240, China

[2] Graduate School of Advanced Science and Engineering, Hiroshima University, Kagamiyama 1-4-1, Higashi, Hiroshima 739-8527, Japan

positioning precision and repeatability of the machine tool [10]. The laser tracker features high measurement precision and a wide measurement range [11], but due to its complex measurement steps and high price, it is mostly used for error calibration of large machine tools [12]. Keaveney et al. took inspiration from high-precision CNC machining systems and used DBB to calibrate 3D printers at a relatively low cost [13]. However, the dimensions of information measured with DBB are relatively limited. The devices mentioned above can effectively perform the error measurement of ordinary CNC machine tools. Nonetheless, their application scenarios are limited to room temperature, so they cannot be used for the error measurement of 3D printers at high temperatures.

At present, the research on geometric error identification for 3D printers is not sufficient. Quantitative analysis of geometric errors of 3D printers is even less, which is largely caused by the bottleneck of the measurement instrument. From the perspective of the use cost of measurement instruments, most of the current options are either quite costly (such as laser trackers and DBB) or cumbersome to operate (such as laser interferometers). More importantly, the above equipment cannot work in high-temperature environments. The above reasons make it quite difficult to accurately measure the geometric errors of 3D printers at high temperatures, but vision measurement, as an economical and remote measurement method, becomes a new option.

In recent years, with the advantages of low cost, easy operation, high measurement efficiency, and wide application scenarios, vision measurement is playing an increasingly important role in the industry [14]. At the same time, there are more and more attempts to apply vision measurement to machine tool error measurement. Ibaraki et al. [15] applied monocular vision to the measurement of two-dimensional errors in the machine tool plane. However, due to the lack of depth information, this method is not suitable for three-dimensional application scenarios. Chen et al. [16] applied visual measurement to PDGE calibration of five-axis machine tools. However, the longitudinal measurement range of this method is relatively limited. Liu et al. [17] applied binocular vision to five-axis machine tools to realize dynamic detection and recognition of PIGEs. However, the research on vision measurement of geometric errors in 3D printers is relatively insufficient, and there are still the following issues that need to be considered. Although vision measurement has been applied to many industrial measurement scenarios, to achieve high-accuracy three-dimensional error measurement is still quite difficult. Vision measurement will introduce additional error factors such as camera distortion, which need to be considered and corrected. And the layout of the measurement system affects the precision and reliability of measurement data. In addition, to measure the geometric error of a 3D printer, interference factors in the actual environment such as space constraints, high temperature, and lighting conditions need to be considered [18]. To achieve geometric error measurement of a 3D printer at high temperatures, a binocular vision measurement system and a rapid error identification algorithm are proposed in this research. Through measurement experiments, it has been proven that the method proposed in this paper is effective and can fill the gap of conventional measurement instruments in high-temperature environments. In addition, the contribution of linear axis error motions on the geometric accuracy of printed workpieces is proven by printing experiments.

The remainder of this paper is organized as follows. In Section 2, the definition of the geometric errors of a three-axis 3D printer is explained. Section 3 explains the recognition process of feature points and the specific principle of binocular vision measurement. In Section 4, the rapid identification algorithm for 21 geometric errors is derived. In Section 5, geometric error measurement is performed on a 3D printer using the proposed method. In addition, a comparative experiment at room temperature is conducted between DBB and the proposed vision measurement system, and an error compensation experiment is conducted to validate the effectiveness of the system. Finally, Section 6 summarizes the contributions of this research.

2 Geometric errors of 3D printer

2.1 Configuration of 3D printer

A large-sized industrial 3D printer produced by INTAMSYS is used in the study, as shown in Fig. 1. It can be regarded as a ZFXY-type machine tool composed of three translational axes (X-, Y-, and Z-axes). The kinematic chain from the workpiece coordinate system to the tool (printhead) coordinate system is as follows: workpiece—Z axis—machine—X axis—Y axis—tool.

2.2 Definition of geometric errors of translational axes

The single-axis movement of a three-axis CNC machine tool can produce six geometric errors: one positioning error, two straightness errors, and three rotary errors. The definition of geometric error in this paper refers to the international standard ISO 230–1:2012. For the X-axis, δ_{xx} represents the X axial deviation, δ_{yx} and δ_{zx} represent the components of the spatial positioning error along the Y-axis and Z-axis directions, respectively; ε_{xx}, ε_{yx}, and ε_{zx} represent the angle at which the worktable rotates about three translational axes, respectively.

Each translational axis of the 3D printer has 6 geometric errors, and there are 18 items in total for the three axes. In

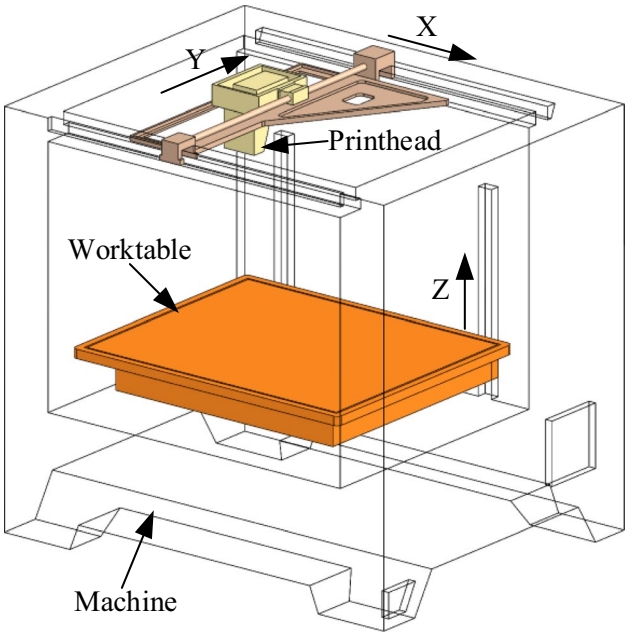

Fig. 1 3D printer configuration

Table 1 Definition of 21 geometric errors

Type	Geometric error
X-axis	δ_{xx}, δ_{yx}, δ_{zx}, ε_{xx}, ε_{yx}, ε_{zx}
Y-axis	δ_{xy}, δ_{yy}, δ_{zy}, ε_{xy}, ε_{yy}, ε_{zy}
Z-axis	δ_{xz}, δ_{yz}, δ_{zz}, ε_{xz}, ε_{yz}, ε_{zz}
Squareness error	S_{xy}, S_{xz}, S_{yz}

addition, the deviation of the angles of each two axes relative to 90° is a squareness error, namely S_{xy}, S_{xz}, and S_{yz}. Therefore, a three-axis 3D printer possesses 21 geometric errors. Table 1 illustrates symbolic representations of geometric errors, which refers to [19].

3 Three-dimensional position measurement based on binocular vision

Binocular vision is utilized to obtain the three-dimensional position of an object. And it can be abstracted into two stages: First, the pixel coordinates of the feature points in the left and right camera images are acquired through image recognition. Then, using the pixel coordinates obtained in the first stage, the coordinate values of these points in the world coordinate system are solved.

3.1 Obtain pixel coordinates using cooperative targets

The ArUco code shown in Fig. 2 is used as the cooperative target to provide identifiable feature points. The pattern can be quickly obtained from the OpenCV library via a coding matrix. The pattern is printed on the aluminum plate as the target and captured by the binocular camera. Using the appropriate recognition algorithm, the pixel coordinates in acquired images of four corner points around the pattern can be obtained. Specifically, the acquired images will go through the steps of image processing, candidate contour search and target recognition successively, so as to accurately identify the peripheral boundary of the target pattern and the four corner points on the boundary, and finally output the pixel coordinates of the four corner points, as shown in Fig. 2.

3.2 Calculate world coordinates based on pixel coordinates

A binocular system with a non-parallel alignment configuration is used in this paper, and its measurement principle is illustrated in Fig. 3. Let the left camera coordinate system and the world coordinate system coincide, and the transformation matrices between left and right cameras be

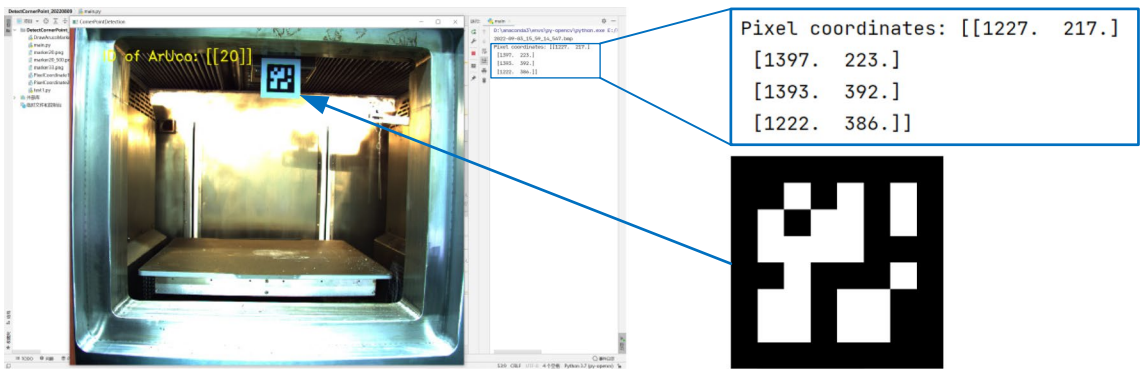

Fig. 2 ArUco code

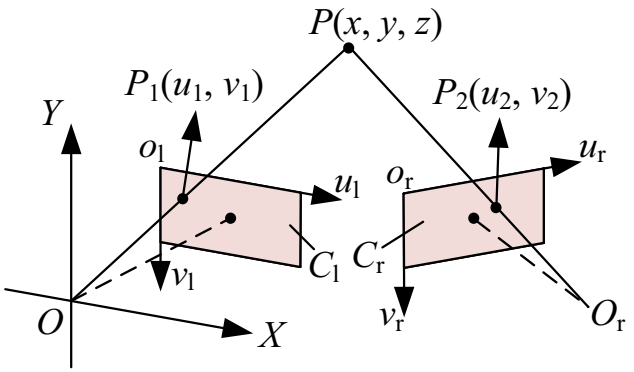

Fig. 3 Ray binocular model

$R = \begin{bmatrix} r_1 & r_2 & r_3 \\ r_4 & r_5 & r_6 \\ r_7 & r_8 & r_9 \end{bmatrix}$ and $T = \begin{bmatrix} t_x \\ t_y \\ t_z \end{bmatrix}$, and the intrinsic parameter matrices of left and right cameras be K_1 and K_2, respectively. Let the world coordinates of any spatial point P be (x, y, z) and the pixel coordinates of point P in the left and right camera images be $p_1(u_1, v_1)$ and $p_2(u_2, v_2)$, respectively. The transformation matrices from pixel coordinates of image points to world coordinates are

$$z_{c1}\begin{bmatrix} u_1 \\ v_1 \\ 1 \end{bmatrix} = M_1 \begin{bmatrix} x \\ y \\ z \\ 1 \end{bmatrix} = \begin{bmatrix} m_{11}^1 & m_{12}^1 & m_{13}^1 & m_{14}^1 \\ m_{21}^1 & m_{22}^1 & m_{23}^1 & m_{24}^1 \\ m_{31}^1 & m_{32}^1 & m_{33}^1 & m_{34}^1 \end{bmatrix} \begin{bmatrix} x \\ y \\ z \\ 1 \end{bmatrix} \tag{1}$$

$$z_{c2}\begin{bmatrix} u_2 \\ v_2 \\ 1 \end{bmatrix} = M_1 \begin{bmatrix} x \\ y \\ z \\ 1 \end{bmatrix} = \begin{bmatrix} m_{11}^2 & m_{12}^2 & m_{13}^2 & m_{14}^2 \\ m_{21}^2 & m_{22}^2 & m_{23}^2 & m_{24}^2 \\ m_{31}^2 & m_{32}^2 & m_{33}^2 & m_{34}^2 \end{bmatrix} \begin{bmatrix} x \\ y \\ z \\ 1 \end{bmatrix} \tag{2}$$

where $M_1 = \left[K_1 0\right]_{3\times4}$, $M_2 = K_2[RT]_{3\times4}$, z_{c1} and z_{c2} are the depth values of point P in the Z direction of the left and right camera coordinate systems, respectively.

According to Eqs. (1) and (2), the following equation can be obtained:

$$\begin{cases} (u_1 m_{31}^1 - m_{11}^1)x + (u_1 m_{32}^1 - m_{12}^1)y + (u_1 m_{33}^1 - m_{13}^1)z = m_{14}^1 - u_1 m_{34}^1 \\ (v_1 m_{31}^1 - m_{21}^1)x + (v_1 m_{32}^1 - m_{22}^1)y + (v_1 m_{33}^1 - m_{23}^1)z = m_{24}^1 - v_1 m_{34}^1 \\ (u_2 m_{31}^2 - m_{11}^2)x + (u_2 m_{32}^2 - m_{12}^2)y + (u_2 m_{33}^2 - m_{13}^2)z = m_{14}^2 - u_2 m_{34}^2 \\ (v_2 m_{31}^2 - m_{21}^2)x + (v_2 m_{32}^2 - m_{22}^2)y + (v_2 m_{33}^2 - m_{23}^2)z = m_{24}^2 - v_2 m_{34}^2 \end{cases} \tag{3}$$

The simplified expression is

$$A_{4\times3}\left[xyz\right]^T = B_{4\times1} \tag{4}$$

These equations contain three unknown numbers (x, y, z) and four equations, which belong to the overdetermined equation. Considering the calibration error and corner extraction error, the least squares solution is used to calculate Eq. (4), which can be represented by

$$\left[xyz\right]^T = \left(A^T A\right)^{-1} A^T B \tag{5}$$

The relevant camera parameter matrices in the above equations can be obtained by binocular camera calibration. In addition, the distortion coefficients of the camera are also determined by the camera calibration and are used to correct the pixel coordinates of the corner points, so as to obtain the pixel coordinates without distortion. In this research, the binocular vision system is calibrated with high accuracy using a high-precision calibration plate with known geometric dimensions based on Zhang's method [20].

4 Calculation of geometric errors

4.1 Comprehensive error model of machine tools

In this section, geometric errors are considered in establishing the kinematics model of the machine tool. Taking the worktable moving x along the X-axis as an example, let the three translational errors of the X-axis be δ_{xx}, δ_{yx}, and δ_{zx}, and the three rotary errors be ε_{xx}, ε_{yx}, and ε_{zx}. The homogeneous transformation matrix from the reference coordinate system to the X-axis coordinate system is

$${}_X^R T^e = \begin{bmatrix} 1 & -\varepsilon_{zx} & \varepsilon_{yx} & x + \delta_{xx} \\ \varepsilon_{zx} & 1 & -\varepsilon_{xx} & \delta_{yx} \\ -\varepsilon_{yx} & \varepsilon_{xx} & 1 & \delta_{zx} \\ 0 & 0 & 0 & 1 \end{bmatrix} \tag{6}$$

Similarly, the transformation matrices corresponding to the Y-axis and Z-axis, namely, ${}_Y^X T^e$ and ${}_R^Z T^e$, can be obtained. When the machine tool undergoes a displacement of x, y, and z along the X, Y, and Z axes, respectively, the transformation relationship between the workpiece coordinate system W and the tool coordinate system T can be expressed as

$${}_T^W T^e = {}_Z^W T^e \cdot {}_R^Z T^e \cdot {}_X^R T^e \cdot {}_Y^X T^e \cdot {}_T^Y T^e \tag{7}$$

where ${}_Z^W T^e$ and ${}_T^Y T^e$ are regarded as identity matrices.

By substituting the transformation matrix of each axis into the above equation, the comprehensive error model of the ZFXY-type machine tool can be obtained as follows:

$$\begin{bmatrix} 1 & -\varepsilon_{zy} - \varepsilon_{zx} + \varepsilon_{zz} & \varepsilon_{yy} + \varepsilon_{yx} - \varepsilon_{yz} & \delta_{xy} - yS_{xy} - y\varepsilon_{zx} + \delta_{xx} + x + y\varepsilon_{zz} - \delta_{xz} - zS_{xz} \\ -\varepsilon_{zz} + \varepsilon_{zx} + \varepsilon_{zy} & 1 & -\varepsilon_{xy} - \varepsilon_{xx} + \varepsilon_{xz} & -x\varepsilon_{zz} + \delta_{yy} + y + \delta_{yx} - \delta_{yz} + zS_{yz} \\ \varepsilon_{yz} - \varepsilon_{yx} - \varepsilon_{yy} & -\varepsilon_{xz} + \varepsilon_{xx} + \varepsilon_{xy} & 1 & x\varepsilon_{yz} - y\varepsilon_{xz} + y\varepsilon_{xx} + \delta_{zy} + \delta_{zx} - \delta_{zz} - z \\ 0 & 0 & 0 & 1 \end{bmatrix} \tag{8}$$

4.2 Abbe principle

Abbe principle is an important theorem in precision measurement, which explicitly stipulates that if the actual functional axis is inconsistent with the measurement axis, the measurement value of translational error should be rectified using the product of the relevant angular error and the offset between the measurement point and the actual functional point [21]. It should be noted that the angular errors remain constant for different points on the same rigid body, while the translational errors vary with position.

Next, the application of the Abbe principle in geometric error measurement of three-axis machine tools will be explained by taking the measurement of worktable B moving along the *X*-axis in the reference coordinate system as an example. The measurement system is installed separately at two points connected to worktable B for measurement. The measured values of the angular error remain unchanged, and the measured values of the translational error will be different because the translational error is affected by the angular error and the position offset.

During worktable movement along the *X*-axis, the effect of the yaw angle of the worktable around the *Z*-axis on the positioning error is as follows:

$$\Delta_{\gamma}(x_i) = tg\gamma(x_i)y_i \approx \gamma(x_i)y_i \tag{9}$$

where x_i is the nominal position, y_i is the offset of the measurement point relative to the reference axis, and $\gamma(x_i)$ is the angular error about the *Z*-axis at x_i. The specific geometric relationship is shown in Fig. 4, where $\Delta_x(x_i)$ refers to $\Delta_{\gamma}(x_i)$ in Eq. (9).

Similar to Eq. (9), the effect of the pitch angle of the worktable around the *Y*-axis on the positioning error is

$$\Delta_{\beta}(x_i) = tg\beta(x_i)z_i \approx \beta(x_i)z_i \tag{10}$$

where x_i is the nominal position, z_i is the offset of the measurement point relative to the reference axis, and $\beta(x_i)$ is the angular error about the *Y*-axis at x_i.

The above two-dimensional results are generalized to three-dimensional space as follows. The measurement systems are installed at selected points b_0 and b_1 on worktable B. Reference coordinate system R and coordinate system B are established with point b_0 as the origin, where R is fixed and B is movable. The coordinates of point b_1 in coordinate system B are (x_1, y_1, z_1). The coordinate systems B_1 and B_2 are established with point b_1 as the origin, where B_1 is fixed and B_2 is movable. In the initial position, R and B coincide, and B_1 and B_2 coincide. The coordinate transformation relation of B_1 to R and B to B_2 is given by the following two equations:

$${}^{R}T_{B_1} = \begin{bmatrix} 1 & 0 & 0 & x_1 \\ 0 & 1 & 0 & y_1 \\ 0 & 0 & 1 & z_1 \\ 0 & 0 & 0 & 1 \end{bmatrix} \tag{11}$$

$${}^{B_2}T_{B} = \begin{bmatrix} 1 & 0 & 0 & -x_1 \\ 0 & 1 & 0 & -y_1 \\ 0 & 0 & 1 & -z_1 \\ 0 & 0 & 0 & 1 \end{bmatrix} \tag{12}$$

When the worktable is displaced by x along the *X*-axis, the relative relationships of coordinate systems R, B_1, B, and B_2 are shown in Fig. 5.

The positioning error δ_{xx} and the straightness error δ_{yx}, δ_{zx} of *X*-axis movement are measured at point b_0. Positioning error δ'_{xx} and straightness error δ'_{yx}, δ'_{zx} of *X*-axis movement are measured at point b_1. According to Eq. (6), the coordinate transformation relation of B to R and B_2 to B_1 is given by the following two equations:

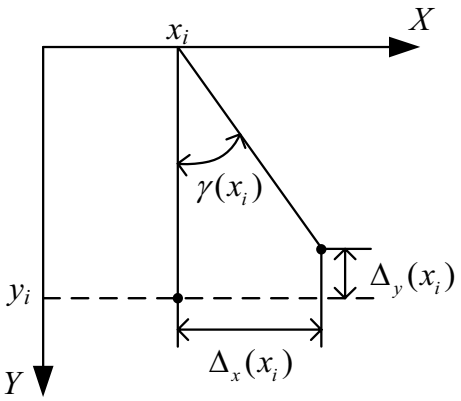

Fig. 4 Line error in *XOY* plane caused by yaw angle

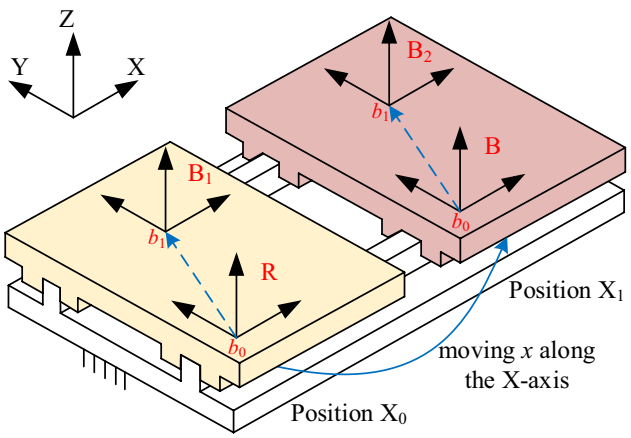

Fig. 5 Relative relation of coordinate systems

$$
{}^{R}T_{B} = \begin{bmatrix} & -\varepsilon_{zx} & \varepsilon_{yx} & x+\delta_{xx} \\ \varepsilon_{zx} & 1 & -\varepsilon_{xx} & \delta_{yx} \\ -\varepsilon_{yx} & \varepsilon_{xx} & 1 & \delta_{zx} \\ 0 & 0 & 0 & 1 \end{bmatrix} \tag{13}
$$

$$
{}^{B_1}T_{B_2} = \begin{bmatrix} 1 & -\varepsilon_{zx} & \varepsilon_{yx} & x+\delta'_{xx} \\ \varepsilon_{zx} & 1 & -\varepsilon_{xx} & \delta'_{yx} \\ -\varepsilon_{yx} & \varepsilon_{xx} & 1 & \delta'_{zx} \\ 0 & 0 & 0 & 1 \end{bmatrix} \tag{14}
$$

According to the homogeneous transformation method, there are

$$
{}^{R}T_{B} = {}^{R}T_{B_1} \cdot {}^{B_1}T_{B_2} \cdot {}^{B_2}T_{B} \tag{15}
$$

Substitute the four transformation matrices into Eq. (15), and from the equivalence of the corresponding elements of the matrices on both sides of the equation, it can be obtained that

$$
\begin{cases} \delta_{xx} = \delta'_{xx} - \varepsilon_{yx} z_1 + \varepsilon_{zx} y_1 \\ \delta_{yx} = \delta'_{yx} - \varepsilon_{zx} x_1 + \varepsilon_{xx} z_1 \\ \delta_{zx} = \delta'_{zx} - \varepsilon_{xx} y_1 + \varepsilon_{yx} x_1 \end{cases} \tag{16}
$$

From the above equation, it can be obtained that the difference in translational error measured at two measurement points on the same rigid body is equal to the linear combination of the product of the offset and the rotary error between the two measurement points.

4.3 Geometric error identification

In the quick identification method for geometric errors presented in this paper, two targets are connected at regular intervals using a fixture, and the fixture is fixed on the printhead or *Z*-axis platform of the 3D printer. Then, each axis is controlled to move in a fixed step, as shown in Fig. 6. At the same time, a binocular vision system is used to collect real-time images of the targets. The obtained image data are divided into 9 groups and named as lines 1 to 9, as shown in Fig. 6. In order to prevent the high temperature in the chamber from affecting the measurement accuracy of the camera, the measurement process has been optimized so that the time of a single measurement is relatively short.

During experimental data processing, the coordinate values of each measurement point in lines 1 to 9 under the camera coordinate system are calculated based on the camera calibration results and the pixel coordinates of the target corner points identified. The least-square fitting of three-dimensional scatter points on each line is carried out respectively, and the positioning error ΔL of each point in the direction of the fitting line is calculated according to Fig. 7.

According to the positioning error data of lines 1, 2, and 3, calculate the positioning errors of the translational axis according to the following equations:

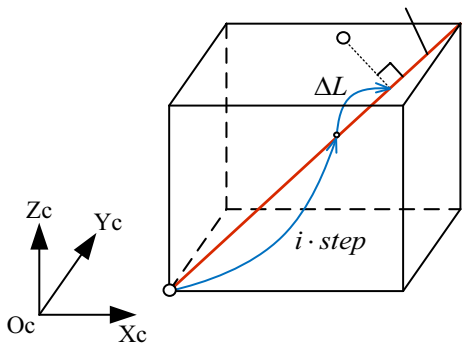

Fig. 7 Calculation method of positioning error

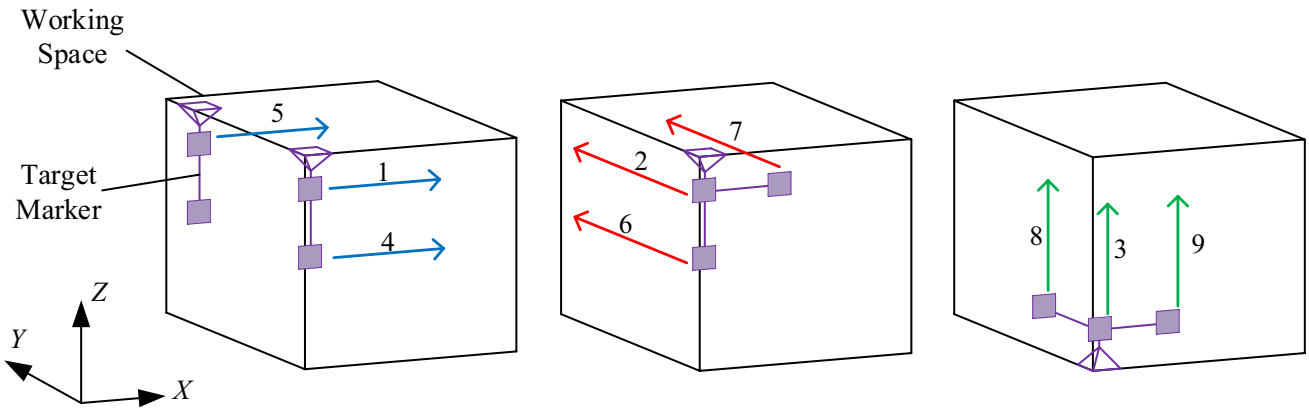

Fig. 6 Distribution of measurement lines

$$\begin{cases} \delta_{xx} = \Delta L(x,0,0) \\ \delta_{yy} = \Delta L(0,y,0) \\ \delta_{zz} = \Delta L(0,0,z) \end{cases} \tag{17}$$

Using the conclusions of Section 4.2, yaw errors and pitch errors of the translation axis are calculated according to the following equations based on the positioning error data of lines 4 to 9:

$$\begin{cases} \varepsilon_{yx} = [\Delta L(x,0,z_0) - \Delta L(x,0,0)]/z_0 \\ \varepsilon_{zx} = [\Delta L(x,0,0) - \Delta L(x,y_0,0)]/y_0 \\ \varepsilon_{xy} = [\Delta L(0,y,0) - \Delta L(0,y,z_0)]/z_0 \\ \varepsilon_{zy} = [\Delta L(x_0,y,0) - \Delta L(0,y,0)]/x_0 \\ \varepsilon_{xz} = [\Delta L(0,y_0,z) - \Delta L(0,0,z)]/y_0 \\ \varepsilon_{yz} = [\Delta L(0,0,z) - \Delta L(x_0,0,z)]/x_0 \end{cases} \tag{18}$$

According to the rotary errors mentioned above, the straightness errors are calculated according to the following equations, which refer to [19]

$$\begin{cases} \delta_{yx} = \int \varepsilon_{zx} dx - L_{yx} = P_{yx} - L_{yx} \\ \delta_{zx} = \int \varepsilon_{yx} dx - L_{zx} = P_{zx} - L_{zx} \\ \delta_{xy} = \int \varepsilon_{zy} dx - L_{xy} = P_{xy} - L_{xy} \\ \delta_{zy} = \int \varepsilon_{xy} dx - L_{zy} = P_{zy} - L_{zy} \\ \delta_{xz} = \int \varepsilon_{yz} dx - L_{xz} = P_{xz} - L_{xz} \\ \delta_{yz} = \int \varepsilon_{xz} dx - L_{yz} = P_{yz} - L_{yz} \end{cases} \tag{19}$$

where P_{uv} is the integral of ε_{wv}, and L_{uv} is the least squares fitting line of P_{uv}.

For the squareness errors S_{xy}, S_{yz}, and S_{xz}, they are calculated by fitting the coordinate values of the measurement points and using the included angle between the fitting lines. Taking S_{xz} as an example, the three-dimensional coordinates of the measurement points calculated from the measurement data of line 1 and line 3 are based on the same world coordinate system (that is, the binocular camera system remains stationary during the measurement process). Therefore, the least squares fitting is performed on the measurement points of line 1 and line 3, respectively, and the included angle between the two fitting lines is calculated as γ. Then, $S_{xz} = \gamma - 90°$.

Using the above method, 18 of the 21 geometric errors are identified, with the remaining 3 roll errors ε_{xx}, ε_{yy}, ε_{zz}. Identifying these three geometric errors requires the use of the machine tool comprehensive error model in Section 4.1. The following takes ε_{xx} as an example for explanation.

When the measurement target is installed on the printhead and only the X-axis moves, the error vector is

$$\begin{aligned} E = & \begin{bmatrix} 1 & -\varepsilon_{zx} & \varepsilon_{yx} & x+\delta_{xx} \\ \varepsilon_{zx} & 1 & -\varepsilon_{xx} & \delta_{yx} \\ -\varepsilon_{yx} & \varepsilon_{xx} & 1 & \delta_{zx} \\ 0 & 0 & 0 & 1 \end{bmatrix} \begin{bmatrix} l_x \\ l_y \\ l_z \\ 1 \end{bmatrix} \\ & - \begin{bmatrix} 1 & 0 & 0 & x \\ 0 & 1 & 0 & 0 \\ 0 & 0 & 1 & 0 \\ 0 & 0 & 0 & 1 \end{bmatrix} \begin{bmatrix} l_x \\ l_y \\ l_z \\ 1 \end{bmatrix} = \begin{bmatrix} -\varepsilon_{zx} l_y + \varepsilon_{yx} l_z + \delta_{xx} \\ \varepsilon_{zx} l_x - \varepsilon_{xx} l_z + \delta_{yx} \\ -\varepsilon_{yx} l_x + \varepsilon_{xx} l_y + \delta_{zx} \\ 0 \end{bmatrix} \end{aligned} \tag{20}$$

where $\left[l_x l_y l_z 1\right]^T$ is the coordinate of the measurement point in the X-axis coordinate system.

From Eq. (20), it can be seen that ε_{xx} is only reflected in the y and z components of the error vector, while based on binocular vision measurement data, only errors along the X-axis and perpendicular to the X-axis can be obtained. The error perpendicular to the X-axis is

$$E_{\perp X} = \sqrt{\left(\varepsilon_{zx} l_x - \varepsilon_{xx} l_z + \delta_{yx}\right)^2 + \left(-\varepsilon_{yx} l_x + \varepsilon_{xx} l_y + \delta_{zx}\right)^2} \tag{21}$$

If an X-axis coordinate system is established with the first measurement point as the origin (that is, the data of δ_{xx}, δ_{yx}, and δ_{zx} is measured at the first measurement point), then $l_x = l_y = 0$. The error perpendicular to the X-axis can be simplified as

$$E_{\perp X} = \sqrt{\left(-\varepsilon_{xx} l_z + \delta_{yx}\right)^2 + {\delta_{zx}}^2} \tag{22}$$

where l_z, δ_{yx}, and δ_{zx} are known quantities, so ε_{xx} can be solved.

5 Experiments and results

5.1 Experimental setup

The binocular vision measurement system built in this paper is shown in Fig. 8. The parameters of the binocular vision system listed in Table 2 are optimized so that the uncertainty of measurement matches the accuracy requirements of the 3D printer. And the cooperative target used in this paper is a 70 mm × 70 mm aluminum oxide plate.

5.2 Identification of geometric errors at high temperatures based on binocular vision

The method presented in Section 4.3 is applied to measure the geometric error of a 3D printer at a high temperature (120 ℃). The offsets of lines 4, 6, 8, and 9, namely x_0, y_0, and z_0 in Eq. (18), are all 200 mm, while the offsets of lines 5 and 7 are 150 mm. Based on the measurement data, the positioning

Fig. 8 Binocular vision measurement system

Table 2 Specification of the binocular vision system

Parameter	Value
Resolution	2448 (H)×2048 (V)
Pixel size	3.45 μm×3.45 μm
Focal length	8 mm
Frame rate	36 fps
Operating temperature	0~45 ℃

errors ΔL of 9 lines can be directly obtained, as shown in Fig. 9. Then, pitch errors, yaw errors, and straightness errors are calculated in sequence based on the above positioning errors, as shown in Fig. 10.

As shown in Table 3 and Fig. 11, the squareness errors and the rolling errors of each axis are further calculated based on the above results.

5.3 Identification accuracy verification at room temperature using DBB

After measuring the geometric errors at room temperature using the proposed method, the identification accuracy is verified by using the Renishaw QC20 double-ball bar system. Specifically, we fix the base of DBB on the *Z*-axis platform, fix the moving end on the printhead, as shown in Fig. 12, and control the printhead to make a circumferential motion in the *XOY* plane.

Export the test file from the DBB system, and draw a result graph, as shown in Fig. 13. The measured circular deviation of the error trace is 0.2058 mm.

Then, geometric errors of *X*- and *Y*-axes of the 3D printer are measured at room temperature using the proposed measurement system and method. On the basis of the comprehensive error model in Section 4.1, when only *X*/*Y* axis motion is considered, the actual coordinates are calculated using the following equation:

$$\begin{bmatrix} x' \\ y' \end{bmatrix} = \begin{bmatrix} x + \delta_{xx} + \delta_{xy} - y\varepsilon_{zx} \\ y + \delta_{yx} + \delta_{yy} \end{bmatrix} \tag{23}$$

where x, y are nominal coordinates, and x',y' are actual coordinates.

Using the measurement results based on binocular vision, calculate the actual coordinate values for each point on a circle with a semidiameter of 100 mm and a center of

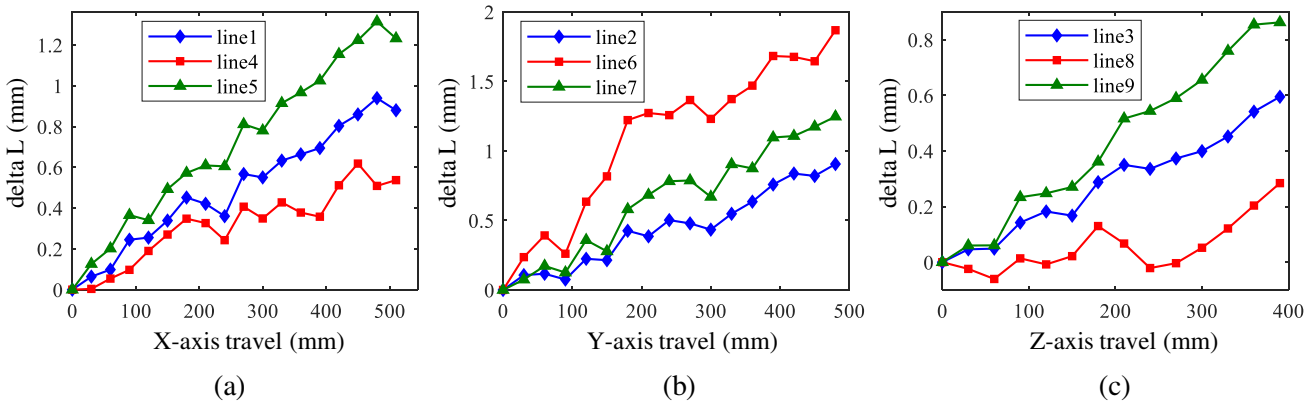

Fig. 9 Measured positioning errors of 9 lines

(212 mm, 270 mm) under the reference coordinate system,

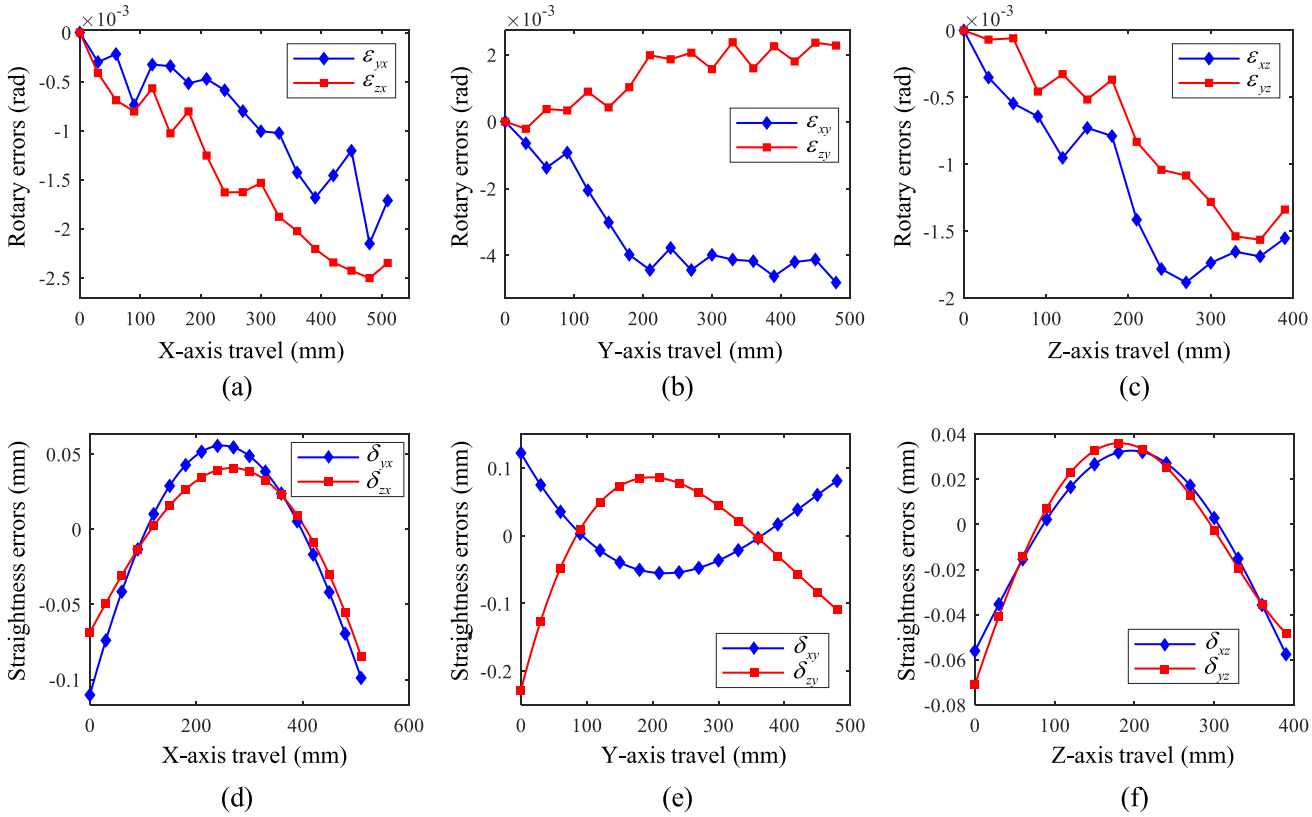

Fig. 10 Calculated rotary errors and straightness errors

Table 3 Calculated squareness errors

Squareness error	Error value (rad)
S_{xy}	-5.05×10^{-3}
S_{xz}	1.24×10^{-3}
S_{yz}	3.84×10^{-3}

taking geometric errors into account. Calculate the difference between 100 mm and the actual distance from each point on the above circle to the center, and draw the error trace using the same method as Fig. 13. The result graph is shown in Fig. 14. The calculated circular deviation of the error trace is 0.1963 mm.

From the above experimental results, the error trace generated based on the geometric error measurement results is in good agreement with the result measured by DBB. Also, the circular deviation calculated based on geometric error is very close to the circular deviation measured by DBB. Therefore, the proposed error measurement method is feasible.

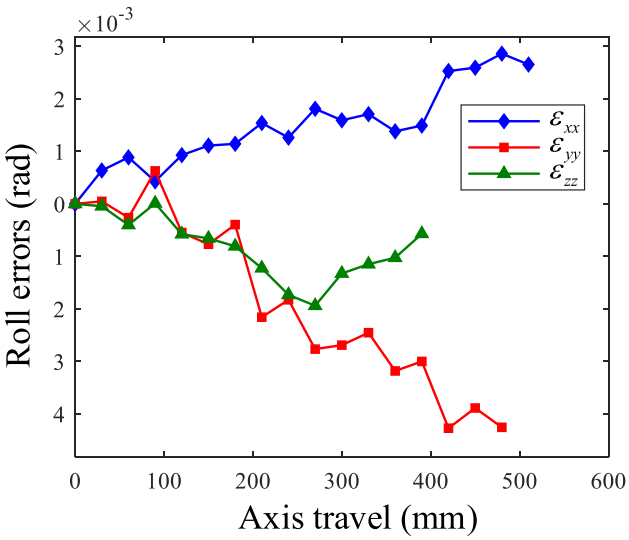

Fig. 11 Calculated roll errors

Fig. 12 DBB measurement experiment

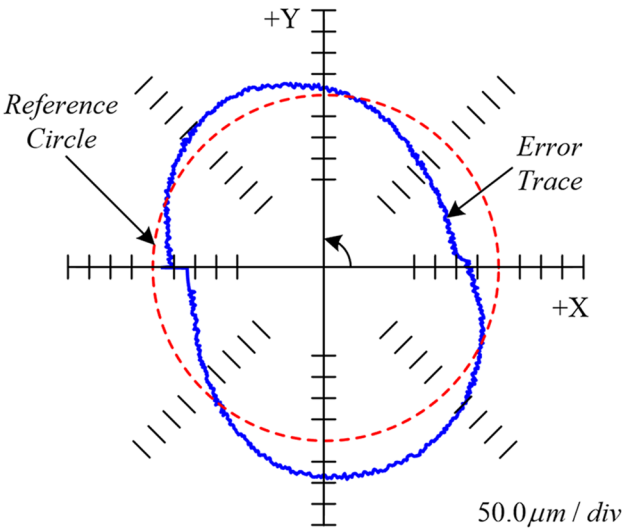

Fig. 13 Experiment result of DBB

5.4 Error compensation experiment

In this section, an error compensation experiment is conducted through actual printing processing. The pattern shown in Fig. 15 is used for printing, and the error compensation is carried out based on the geometric error measurement results in Section 5.2. Two-dimensional patterns before and after compensation are printed respectively and measured to evaluate the accuracy before and after compensation.

A basic compensation algorithm for CNC machining [22] is used in this section. First, reverse post-processing is performed to get the expressions of tool point (x, y, z) about NC code (X, Y, Z) and geometric error quantities:

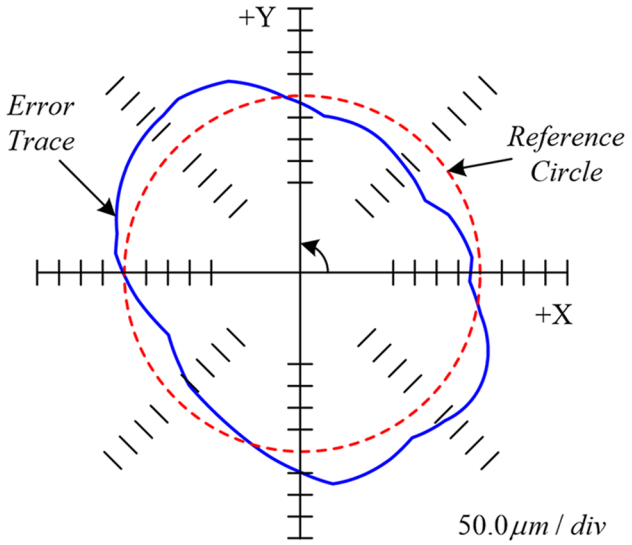

Fig. 14 Calculation results based on geometric error

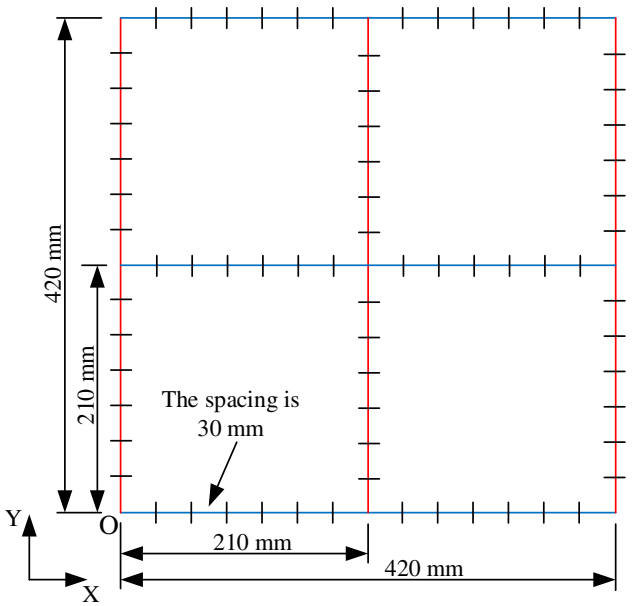

Fig. 15 Patterns for compensation experiments

$$\begin{cases} x = F_x'(X, Y, Z) \\ y = F_y'(X, Y, Z) \\ z = F_z'(X, Y, Z) \end{cases} \tag{24}$$

Calculate the partial differential of the above equation, and use the Jacobi matrix to express the differential relationship:

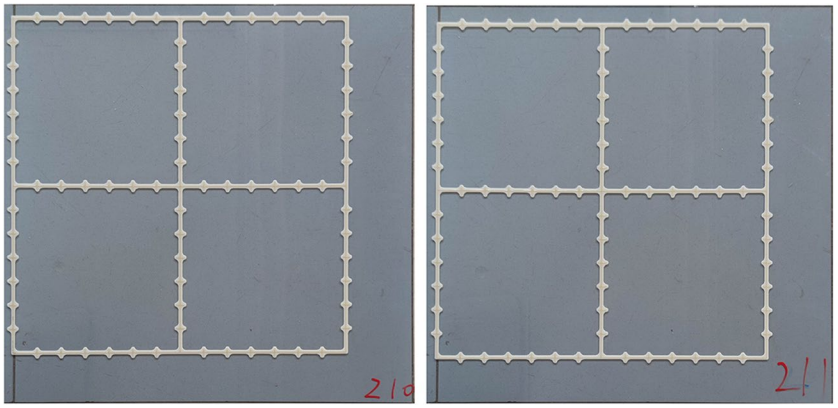

Fig. 16 Workpiece in error compensation experiment

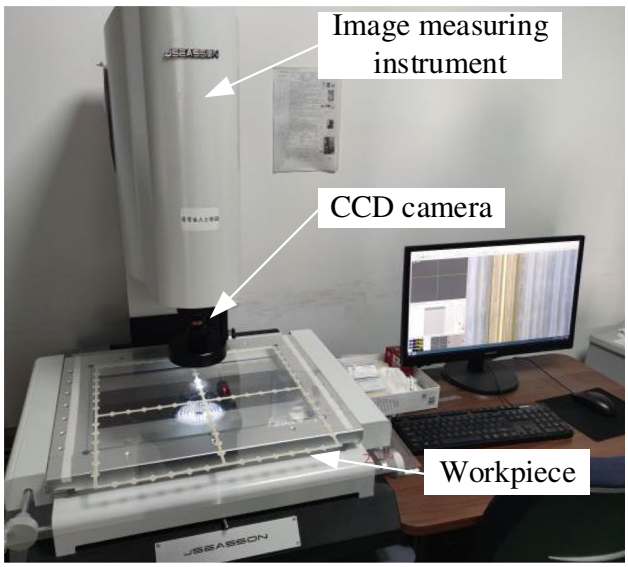

Fig. 17 Workpiece measurement based on image measuring instrument

$$\begin{bmatrix} dx \\ dy \\ dz \end{bmatrix} = \mathrm{J}(X, Y, Z) \begin{bmatrix} dX \\ dY \\ dZ \end{bmatrix} \tag{25}$$

Transform the above equation to obtain

$$\begin{bmatrix} dX \\ dY \\ dZ \end{bmatrix} = \mathrm{J}^{-1}(X, Y, Z) \begin{bmatrix} dx \\ dy \\ dz \end{bmatrix} \tag{26}$$

Let (x, y, z) be the ideal tool position, (X, Y, Z) be the NC code obtained based on the ideal post-processing, (x', y', z') be the actual tool position considering geometric errors, and (X^*, Y^*, Z^*) be the compensated NC code. The error compensation equation is

Table 4 Relative positioning errors before and after compensation

Group	RMSE (m)
Horizontal group, before compensation	2.15×10^{-3}
Vertical group, before compensation	2.53×10^{-3}
Horizontal group, after compensation	1.96×10^{-3}
Vertical group, after compensation	2.17×10^{-3}

$$\begin{bmatrix} X^* \\ Y^* \\ Z^* \end{bmatrix} = \begin{bmatrix} X \\ Y \\ Z \end{bmatrix} - \mathrm{J}^{-1}(X, Y, Z) \begin{bmatrix} x' - x \\ y' - y \\ z' - z \end{bmatrix} \tag{27}$$

The workpiece of the error compensation experiment is shown in Fig. 16.

As shown in Fig. 17, using an image measuring instrument to measure the workpiece, printing errors of measurement points before and after error compensation is obtained. The positioning error of the measurement point relative to the starting point of the long line in which it is located is taken as the relative positioning error. The measurement points are divided into horizontal and vertical groups, denoted in blue and red, respectively, in Fig. 15. Root mean square error (RMSE) is used to evaluate the overall error level of each group. The relative positioning errors before and after compensation are shown in Table 4. According to the experimental data, the effect of error compensation on the reduction of the overall error level in additive manufacturing is considerable.

It should be noted that in addition to geometric errors of the 3D printer, other relevant factors can also affect the accuracy of material extrusion-based additive manufacturing of plastic materials, such as the unevenness of the extruded semi-molten material, material shrinkage and distortions in the solidification of the fused polymer, the

deformation of the printhead, and the uncertainty of visual measurement. Therefore, considering the complexity of the manufacturing process, the above error compensation results are acceptable.

6 Conclusion

This paper proposes a binocular vision measurement system suitable for high-temperature conditions in 3D printers and proposes an identification method to calculate geometric errors. The system collects images of targets fixed to the translational axis and ultimately calculates the geometric errors. The performance of the vision system is verified by the comparison test with DBB and the actual processing test. The measurement results of the vision system can be used to compensate for geometric errors in the translational axes of the 3D printer. The possible uncertainty factors in error measurement and compensation experiments are discussed.

To sum up, a feasible and fast measurement method is proposed for 3D printer geometric errors under high-temperature conditions. In the future, we will use the error measurement results to perform error compensation for the processing of complex workpieces and use a laser interferometer to further validate and optimize the proposed error measurement method. More research will be conducted to improve the accuracy and reliability of the vision measurement system. Although current vision devices are not mature enough, with the optimization of device measurement parameters and visual recognition algorithms, they will show increasing potential in the actual manufacturing process of 3D printers.

Funding The authors gratefully acknowledge the financial support of the National Natural Science Foundation of China (No. 52075337) and the State Key Laboratory of Mechanical System and Vibration (No. MSVZD202113).

Data availability Not applicable.

Code availability Not applicable.

Declarations

Ethics approval Not applicable.

Consent to participate The authors declare that all the authors listed in the article have no objections.

Consent for publication The authors confirm that this work has not been published before and do not consider other places. All co-authors have approved its publication in Springer's corresponding English-language journal.

Competing interests The authors declare no competing interests.

References

1. Lin Z, Fu J, Shen H, Gan W (2014) Non-singular tool path planning by translating tool orientations in C-space. Int J Adv Manuf Technol 71:1835–1848
2. Huang N, Zhang Y, Zhu L, Ibaraki S (2022) Visually quantifiable test piece for five-axis machine tools thermal effects. J Manuf Sci Eng 144(5):054501
3. Tian W, Gao W, Zhang D, Huang T (2014) A general approach for error modeling of machine tools. Int J Mach Tools Manuf 79:17–23
4. Qiao Y, Chen Y, Yang J, Chen B (2017) A five-axis geometric errors calibration model based on the common perpendicular line (CPL) transformation using the product of exponentials (POE) formula. Int J Mach Tools Manuf 118:49–60
5. Lee DM, Zhu Z, Lee KI, Yang SH (2011) Identification and measurement of geometric errors for a five-axis machine tool with a tilting head using a double ball-bar. Int J Precis Eng Manuf 12:337–343
6. Lee KI, Yang SH (2013) Measurement and verification of position-independent geometric errors of a five-axis machine tool using a double ball-bar. Int J Mach Tools Manuf 70:45–52
7. Xiang S, Yang J, Fan K, Lu H (2016) Multi-machine tools volumetric error generalized modeling and Ethernet-based compensation technique. Proc Inst Mech Eng B J Eng Manuf 230(5):870–882
8. Aguado S, Samper D, Santolaria J, Aguilar JJ (2014) Volumetric verification of multiaxis machine tool using laser tracker. Sci World J 2014:959510
9. Tsutsumi M, Tone S, Kato N, Sato R (2013) Enhancement of geometric accuracy of five-axis machining centers based on identification and compensation of geometric deviations. Int J Mach Tools Manuf 68:11–20
10. Paweł M, Bartosz P (2019) Rapid method to determine accuracy and repeatability of positioning of numerically controlled axes. Int J Mach Tools Manuf 137:1–12
11. Zhao D, Bi Y, Ke Y (2017) An efficient error compensation method for coordinated CNC five-axis machine tools. Int J Mach Tools Manuf 123:105–115
12. Ibaraki S, Knapp W (2012) Indirect measurement of volumetric accuracy for three-axis and five-axis machine tools: a review. Int J Autom Technol 6(2):110–124
13. Keaveney S, Connolly P, O'Cearbhaill ED (2018) Kinematic error modeling and error compensation of desktop 3D printer. Nanotechnol Precis Eng 1(3):180–186
14. Yin S, Zhou H (2022) A vision-based error identification method for separating geometric errors of rotating axes in five-axis platforms. Measurement 205:112185
15. Ibaraki S, Tanizawa Y (2011) Vision-based measurement of two-dimensional positioning errors of machine tools. J Adv Mech Des Syst Manuf 5(4):315–328
16. Chen W, Li B, Zhao T, Zhang H, Ye P (2022) Vision measurement system for position-dependent geometric error calibration of five-axis machine tools. Int J Adv Manuf Technol 123(11–12):3969–3981
17. Liu W, Li X, Jia Z, Li H, Ma X, Yan H, Ma J (2018) Binocular-vision-based error detection system and identification method for PIGEs of rotary axis in five-axis machine tool. Precis Eng 51:208–222
18. Liu Y, Guo L, Gao H, You Z, Ye Y, Zhang B (2022) Machine vision based condition monitoring and fault diagnosis of machine tools using information from machined surface texture: a review. Mech Syst Signal Process 164:108068

19. Chen G, Yuan J, Ni J (2001) A displacement measurement approach for machine geometric error assessment. Int J Mach Tools Manuf 41(1):149–161
20. Zhang Z (2000) A flexible new technique for camera calibration. IEEE Trans Pattern Anal Mach Intell 22(11):1330–1334
21. Huang YB, Fan KC, Lou ZF, Sun W (2020) A novel modeling of volumetric errors of three-axis machine tools based on Abbe and Bryan principles. Int J Mach Tools Manuf 151:103527
22. Huang N, Jin Y, Bi Q, Wang Y (2015) Integrated post-processor for 5-axis machine tools with geometric errors compensation. Int J Mach Tools Manuf 94:65–73